CrystEngComm

Cite this: *CrystEngComm*, 2012, **14**, 5493–5504

www.rsc.org/crystengcomm

PAPER

Tuning the magnetic properties of transition metal MOFs by metal–oxygen condensation control: the relation between synthesis temperature, SBU nuclearity and carboxylate geometry†

Maria C. Bernini,[ab] Ana E. Platero-Prats,[a] Natalia Snejko,[a] Enrique Gutiérrez-Puebla,[a] Ana Labrador,[c] Regino Sáez-Puche,[d] Julio Romero de Paz[e] and M. Angeles Monge[a]

Received 22nd November 2011, Accepted 12th May 2012
DOI: 10.1039/c2ce06563k

Five novel metal organic frameworks, belonging to three structural types, have been obtained hydrothermally. Three of them, with formula **[M_3(hfipbb)$_2$(OH)$_2$(H_2O)]** (M = Mn, Co, Ni; hfipbb = 4,4′-(hexafluoroisopropylidene)bis(benzoate) dianion) belong to the first structural type. The crystal structure of the Mn-based compound was obtained from single crystal synchrotron X-ray diffraction data, while the isostructural compounds of Co and Ni were studied by means of Rietveld analysis using powder X-ray diffraction data. The magnetic behavior of the compounds with M = Co and Ni is characterized by the onset of long-range ferromagnetic order at very low temperature with Curie temperatures near 8 and 2.5 K, respectively. Such spontaneous magnetization seems to be preceded by low-dimensional magnetic interactions, due to the nature of the secondary building units (SBUs) of the structure, which are triple chains built by M_3O_{14} units. Structural and topological analyses of **[Mn_2(hfipbb)$_2$(H_2hfipbb)]** and **[Co_2(hfipbb)$_2$(H_2hfipbb)]** (**2** and **3** structural types, respectively; H_2hfipbb = 4,4′-(hexafluoroisopropylidene)bis(benzoic acid)) demonstrate that the packing of the rod-shaped SBUs in **2** prevents the framework interpenetration giving rise to a **bnn** net whereas **3** is a 2-fold interpenetrated **pcu** net with isolated paddle-wheel clusters as SBUs **pcu**. Concerning the magnetic behavior of **2** and **3**, antiferromagnetic interactions observed at very low temperature (magnetic susceptibility maximum at 2.8 and 18 K, respectively) are confined to the secondary building units.

1 Introduction

Metal–organic framework (MOF) materials are constantly attracting significant attention not only for their potential applications as functional crystalline materials, but also for their fascinating topologies and structural diversity.[1] The use of flexible and extended ligands contributes to the development of porous frameworks with diverse structural topologies, which, in turn, can lead to different properties, even for the same constitutive units.

In our group we have successfully explored the use of the bent ligand 4,4′-(hexafluoroisopropylidene)bis(benzoic acid), H_2hfipbb, and we have obtained various 2D and 3D MOFs using alkaline earth (Ca^2), post-transition (Zn^3), p-block (In^4) and rare earth ($Ln^{5,6}$) metal ions. In this way, we decided to proceed with our studies by obtaining MOF materials constructed of the H_2hfipbb ligand and transition metal (TM) ions due to the fact that the compounds of TMs have proved to be excellent catalysts[7] as well as to possess interesting magnetic properties.[8] The discovery of new open-framework structures and topologies, and development of new porous solids with open-shell metal ions, brought in the possibility to obtain nanoporous materials with additional magnetic properties. The synergism of both magnetic properties and specific characteristics of nanoporous materials opens a new route to produce low-density magnetic materials, magnetic sensors and multifunctional or intelligent materials at the nanometer scale.[9,10]

In MOFs, the magnetism may be introduced through the incorporation of magnetic moment carriers such as paramagnetic metals, or open-shell organic ligands, or both.[11] This, in itself, is not enough to render a material magnetic, due to the fact that the magnetism is a cooperative phenomenon and thus requires some kind of exchange between the moment carriers. Therefore, a connection between moment carriers at distances

[a]*Instituto de Ciencia de Materiales de Madrid, ICMM-CSIC, Madrid, Spain. E-mail: amonge@icmm.csic.es*
[b]*Área de Química General e Inorgánica "Dr G.F. Puelles" Facultad de Química, Bioquímica y Farmacia, Chacabuco y Pedernera, Universidad Nacional de San Luis, 5700 San Luis, Argentina*
[c]*BM16-LLS European Synchrotron Radiation Facility, 6 Rue Jules Horowitz-BP 2208043 Grenoble CEDEX 9, France*
[d]*Departamento de Química Inorgánica, Facultad de Ciencias Químicas, Universidad Complutense de Madrid, Ciudad Universitaria s/n, 28040-Madrid, Spain*
[e]*C.A.I. Técnicas Físicas, Facultad de Ciencias Físicas, Universidad Complutense de Madrid, Ciudad Universitaria s/n, 28040-Madrid, Spain*
† Electronic supplementary information (ESI) available: Fig. S1–S10 and Tables S1–3. CCDC reference numbers 842411–842413, 842415 and 842416. For ESI and crystallographic data in CIF or other electronic format see DOI: 10.1039/c2ce06563k

within interacting range is necessary.[12] Regarding that, the carboxylic-based and nitrogen-based ligands have proved to have good super-exchange pathways for magnetic couplings.[9,13] When the inorganic part is a transition element, preferably the 3*d* ones, one might expect to observe magnetic behavior that combines the porous nature of the solid. Regarding the use of such materials, these magnetic porous solids could find interesting applications, for example, for air separation.[14]

Taking into account crystal engineering trends, we have selected the H_2hfipbb ligand and the TM ions Mn(II), Co(II) and Ni(II) in order to obtain open frameworks with magnetic moment carriers. In addition, we have explored several synthesis conditions to expand the possibilities of obtaining diverse crystal topologies with different magnetic properties.

Five novel compounds have been obtained; their structural and magnetic characterization is reported here.

2 Experimental

2.1 General synthesis procedure

[Mn_3(hfipbb)$_2$(OH)$_2$(H_2O)] (1a). This compound was obtained by hydrothermal reaction of 1 mmol of $MnCl_2{\cdot}4H_2O$ with 0.7 mmol of the ligand 4,4′-(hexafluoroisopropylidene)bis(benzoic acid) (H_2hfipbb = $C_{17}H_{10}O_4F_6$) in a mixture of water (5 mL) and triethanolamine (1 mL). The mixture with a starting pH value of 8.5 was heated in a Teflon-lined digestion bomb at 220 °C for five hours and then cooled to room temperature. The pH value at the end of the process was 7.3. Colorless needle-prismatic crystals were collected after washing with distilled water and acetone (yield 62.3%).

[Co_3(hfipbb)$_2$(OH)$_2$(H_2O)] and [Ni_3(hfipbb)$_2$(OH)$_2$(H_2O)] (1b and 1c, respectively). The compounds were obtained by hydrothermal reaction of 0.5 mmol of $CoCl_2{\cdot}6H_2O$ with 0.5 mmol of H_2hfipbb (compound **1b**), or 0.5 mmol of $Ni(NO_3)_2{\cdot}6H_2O$ with 0.8 mmol of H_2hfipbb (compound **1c**), in 6 mL of water with 0.2–0.3 mL of triethylamine (TEA). The mixtures with an initial pH value of 6.1 were heated in Teflon-lined digestion bombs at 200 °C for 7 days and then cooled to room temperature. The pH value at the end of the procedure was 4.9 in the case of **1b** and 4.3 for **1c**. Purple (**1b**, 39.9% yield) and green (**1c**, 76% yield) crystalline powders were collected after washing with distilled water and acetone.

[Mn_2(hfipbb)$_2$(H_2hfipbb)] (2). (**2**) was obtained by reaction of 0.25 mmol of $MnCl_2{\cdot}4H_2O$ with 1.02 mmol of H_2hfipbb in 6 mL of water with the addition of 0.1 mL of TEA. The mixture with a starting pH value of 6.3 was heated for 24 h in a Teflon-lined digestion bomb at 170 °C and then cooled to room temperature. The pH value at the end of the process was 5.0. Colorless prismatic crystals were collected after washing with distilled water and acetone (yield 71%).

[Co_2(hfipbb)$_2$(H_2hfipbb)] (3). This compound was obtained by reaction of 1 mmol of $CoCl_2{\cdot}6H_2O$ with 0.8 mmol of H_2hfipbb in 6 mL of water with the addition of 0.05 mL of TEA. This mixture was heated in a Teflon-lined digestion bomb at 170 °C for 6 days and then cooled to room temperature. Dark gray prismatic crystals were collected after washing with distilled water and acetone. In such conditions the obtained yield is 30.47%. If the amount of TEA is augmented to 0.15 mL, the resultant yield is 57.26% with the obtained crystals being of bigger size.

2.2 Characterization

Elemental analysis. Compound **1a**, % C: calc. 40.90, found 40.98, % H: calc. 2.00, found 1.99. Compound **1b**, % C: calc. 39.38, found 38.90, % H: calc. 2.32, found 2.01. Compound **1c**, % C: calc. 40.42, found 40.37, % H: calc. 1.98, found 1.94. Compound **2**: C: calc. 47.75, found 46.63, % H: calc. 1.95, found 1.96. Compound **3**, % C: calc. 47.49, found 46.56, % H: calc. 1.94, found 2.01.

Single-crystal structure determination and refinement. X-ray diffraction data on a single crystal of compound **1a** of dimensions 0.08 × 0.02 × 0.02 mm^3 was collected at the ESRF synchrotron BM16 beam line (Grenoble, France) using λ = 0.7378 Å at 100 K. Data were indexed, integrated, and scaled using the HKL2000 program.[15]

Appropriated single crystals of compounds **2** and **3** were mounted on a Bruker four circle kappa-diffractometer equipped with a Cu INCOATEC microsource operated at 30 W power (45 kV, 0.60 mA) to generate Cu-Kα radiation (λ = 1.54178 Å), and a Bruker AXIOM area detector (microgap technology). Diffraction data were collected over a hemisphere of reciprocal space in a combination of phi and omega scans to reach a resolution of 0.8 Å (58.91° in θ), using a Bruker APEX2 software suite (each exposure of 10 s covered 0.5° in ω). Unit cell dimensions were determined by a least-squares fit of reflections with $I > 2\sigma(I)$. The structures were solved by direct methods and refined by anisotropic full-matrix least-squares, except for hydrogen atoms, as $P2_1/c$ (compound **1a**), as $C2/c$ (compound **2**) or $P2/n$ (compound **3**) space groups. A summary of the conditions for data collection and structure refinement is given in Table 1 (compounds **1a** and **2**) and Table S1† (compound **3**). All calculations were performed using: SMART software for data collection; SAINT plus program[16] for integration and scale correction of data; SHELXTL[17] to resolve and refine the structure and to prepare material for publication; and ATOMS[18] for molecular graphics.

X-ray powder diffraction data. X-ray powder diffraction (XRPD) measurements were performed with a Bruker D8 diffractometer in the θ–θ mode using nickel-filtered Cu-K$\alpha_{1,2}$ (λ = 0.15418 nm) radiation. The best counting statistics were achieved by using a scanning step of 0.02° was taken between Bragg angles of 5 and 40° with an exposure time of 2 s per step.

The purity of all compounds was confirmed by comparison of the simulated and experimental PDRX patterns (see Figures S1–S3 in Supporting Information†) along with the elemental analysis results.

X-Ray powder data refinements: powder patterns of compounds **1a–c** were refined by the Rietveld method (from 2θ = 5–30°) using the Materials Studio software.[19]

Thermogravimetric and differential thermal analyses (TGA/DTA). These measurements were performed using a SEIKO TG/

Table 1 Main crystallographic and refinement data for compounds **1a** and **2**

	Compound **1a**	Compound **2**
Formula	$[Mn_3C_{34}H_{20}O_{11}F_{12}]$	$[Mn_2C_{51}H_{25}O_{12}F_{18}]$
T/K	100(2)	296(2)
Molecular weight/g mol^{-1}	997.32	1281.59
Crystal system	Monoclinic	Monoclinic
Space group	$P2_1/c$	$C2/c$
a/Å	7.277(1)	31.934(1)
b/Å	31.837(6)	7.3362(3)
c/Å	16.434(3)	22.495(1)
α (°)	90	90
β (°)	99.98(3)	95.275(2)
γ (°)	90	90
V/Å^3	3749.8(1)	5247.7(4)
Z	4	4
D_c/g cm^{-3}	1.767	1.622
μ/mm^{-1}	1.114	5.062
Dimensions/mm	0.08 × 0.02 × 0.02	0.6 × 0.14 × 0.02
Limiting indices h	$0 < h < 10$	$-36 < h < 36$
k	$0 < k < 46$	$-8 < k < 5$
l	$-23 < l < 23$	$-25 < l < 25$
F(000)	1980	2556
Reflections collected/unique with $I > 2\sigma(I)$	10 992/7367	4101/3290
Refined parameters	566	427
Goodness-of-fit on F^2	1.040	1.145
R_1	0.0664	0.0399
wR_2	0.2034	0.1169
R-factor-all	0.1043	0.0526

DTA 320 apparatus in the temperature range 25–900 °C in air (flow of 100 mL min^{-1}) at a heating rate of 10 °C min^{-1}. In the case of compound **2**, an additional measurement was performed in the range 25–600 °C employing a heating rate of 5 °C min^{-1} up to 300 °C and 2 °C min^{-1} from 300 °C to 600 °C in order to improve the DTA peak definition associated with the observed thermogravimetric processes in this temperature zone.

Infrared spectroscopy. The IR spectra were recorded from KBr pellets in the range 4000–250 cm^{-1} on a Perkin-Elmer spectrometer.

Magnetic measurements. The dc and ac magnetization measurements were carried out on polycrystalline samples using a superconducting quantum interference device (SQUID) magnetometer (Quantum Design, model MPMS-XL). The data were obtained after cooling in the absence of an external magnetic field. The thermal variation of dc magnetic susceptibility, χ, was obtained in the temperature range 2–300 K with an applied magnetic field of 0.1 T. The temperature dependence of the ac magnetic susceptibility χ_{ac} was obtained in the temperature range 2–180 K, in the absence of an external magnetic field, by means of applying an oscillating magnetic field with a drive amplitude of 3.5 Oe at 20 and 200 Hz. The magnetic field dependence of the dc magnetization was obtained at 2 K up to ± 50 kOe. The diamagnetic contribution was subtracted from the experimental susceptibilities.[20]

3 Results and discussion

3.1 Crystal structure descriptions

[Mn_3(hfipbb)$_2$(OH)$_2$(H_2O)] (compound 1a). This compound crystallizes in the monoclinic system, space group $P2_1/c$. In the asymmetric unit there are four Mn(II) ions which are crystallographically non-equivalent, two of them located in −1 special positions, and thus, with a multiplicity of ½. There are also two hfipbb^{2-} anions, two μ_3-OH groups and one coordinated water molecule. All Mn ions have six oxygen atoms in their coordination environments (Fig. 1). The inorganic part of the framework is formed by infinite chains of trimeric Mn_3O_{14} units. Two kinds of edge sharing octahedral trimeric units can be depicted, those formed by Mn1–Mn4–Mn1, whose shared edges are μ(OH)–μ(OH) groups, and thus, with a shorter inter-metallic distance (3.170(9) Å), and those formed by Mn2–Mn3–Mn2 sharing two μ carboxylic oxygen atoms, with an inter-metallic distance of 3.503(1) Å. The connections among trimers are made

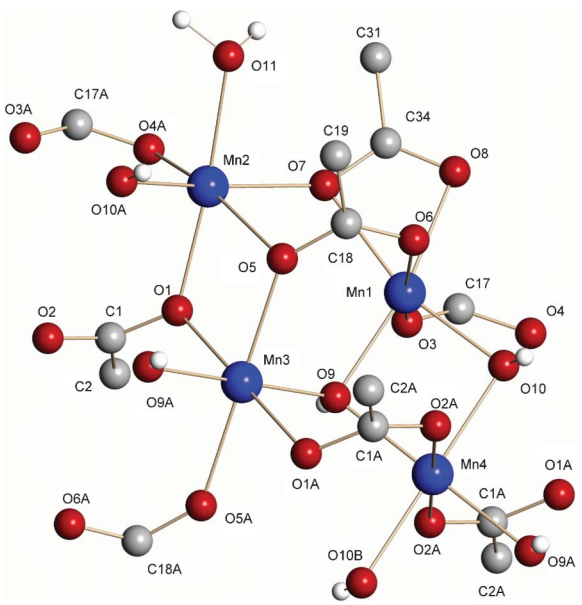

Fig. 1 Coordination spheres of Mn1–Mn4 ions in compound **1a**.

via OH vertex, the latter thus becoming μ_3-OH groups. The distances between metals of different trimers are 3.780(1), 3.540(1), 3.504(1), 3.690(1), and 3.6385(8) Å, for Mn1···Mn2, Mn1···Mn2a, Mn1···Mn3, Mn2···Mn4 and Mn3···Mn4, respectively.

These triple chains that extend in the *a* direction constitute the secondary building unit (SBU) and are linked to each other by the L1 and L2 ligands, giving rise to the 3D metal organic framework (see Fig. 5 left).

One of the hfipbb^{2-} anions, named L1 from now on, connects five metal centers through its two carboxylate groups. In this way, it acts as a tridentate bridge by one carboxylate group linking Mn1, Mn2 and Mn3, and as a chelate-bridge by the other one coordinating at Mn1 and Mn2. In Scheme 1 are shown the coordination modes and the most important geometric features (distance between the carboxylate groups "*d*" and angle between aromatic rings "ω") that are exhibited by the 4,4′-(hexafluoroisopropylidene)bis(benzoic) acid ligand in compounds **1–3**.

The other hfipbb^{2-} anion, L2, also connects five Mn ions; it has a tridentate bridge carboxylate group that links at the Mn4, Mn3 and Mn2 ions and the other carboxylate group acts as a bidentate bridge, linking at the Mn1 and Mn2 ions.

The L1 anion generates a rhomboidal channel whose diagonals are of approximately 28.3 Å × 16.4 Å size. Two

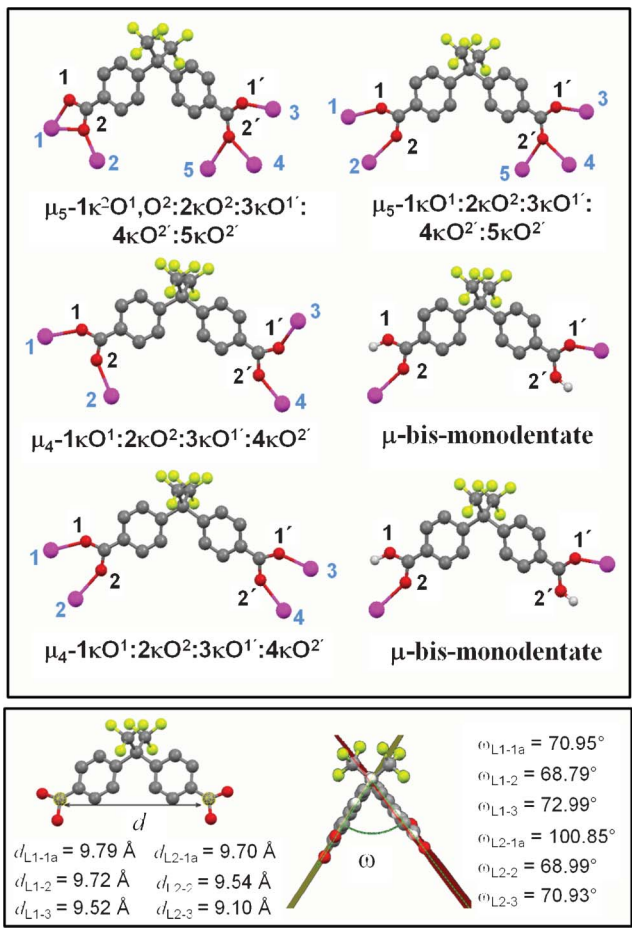

Scheme 1 Top: coordination modes of the L1 (left) and L2 (right) ligands in compounds **1** (top), **2** (middle) and **3** (bottom). Bottom: definition of *d* distance (left) and ω angle (right).

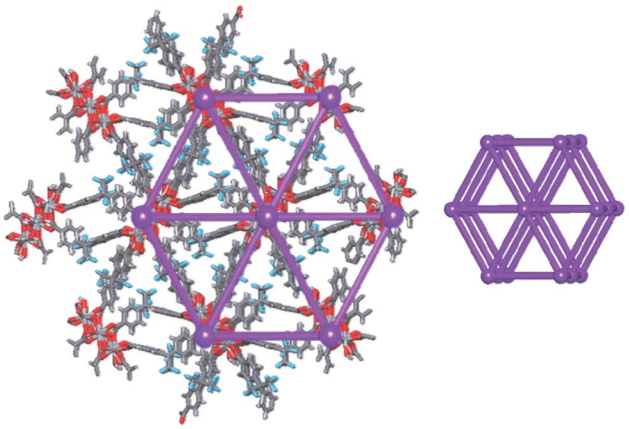

Fig. 2 Projection of hexagonal packing of flat triple chains in compound **1** along the [100] direction.

molecules of L2 are situated inside this cavity along the shortest diagonal. In this way, L1 develops the main channel, which is occupied by the L2 ligand that, in turn, determines another smaller channel. The opposite walls (aromatic rings) of this channel are perfectly parallel.

From a topological point of view, compound **1** consists on a multinodal complex net, so the best description is indeed as packing flat triple chains and as can be seen in Fig. 2, it looks like a "hex" rod packing.

[Mn_2(hfipbb)$_2$(H_2hfipbb)] (2). This compound crystallizes in the monoclinic system, space group *C*2/*c*. In the asymmetric unit there is one Mn(II) ion, one hfipbb ligand (L1) and half a H_2hfipbb ligand (L2).

The Mn ion is surrounded by five O atoms coming from the hfipbb (L1) and H_2hfipbb (L2) ligands in a pyramidal geometry (Fig. 3).

The L1 ligand coordinates four Mn ions through its bis-(bidentate-bridge) coordination mode. This linker is located along the *c* direction, and each carboxylate group exhibits a

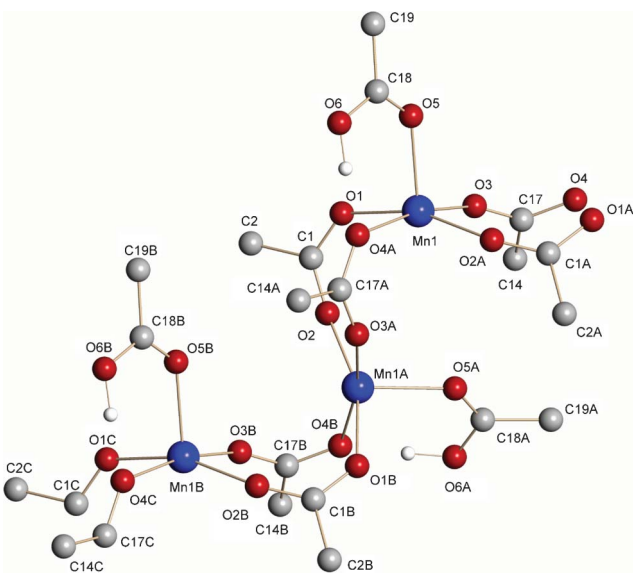

Fig. 3 Coordination environment of one Mn(II) ion in compound **2**.

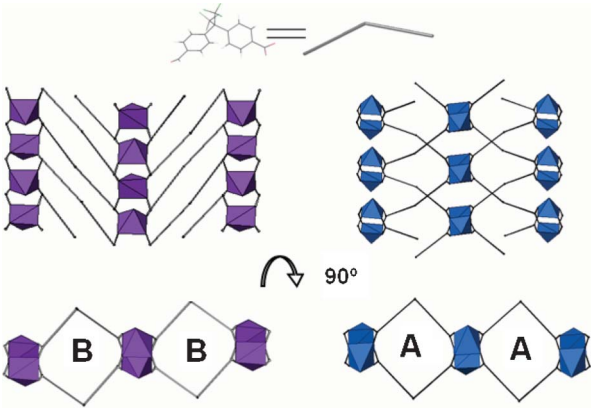

Fig. 4 Two types of channels in: (left) parallel connections in **2**, (right) edge crossing connections in **3** structural types.

syn-anti geometry (Scheme 1). In turn, each carboxylate group of this ligand links the MnO_5 pyramids along the *b* direction giving rise to the formation of chains. The metallic chains are connected through the ligand anions in a parallel way, forming B type channels[21] (Fig. 4), and these linkages among chains in the *c* direction give rise (*via* L1 ligands) to thick layers perpendicular to the *a* direction. Due to the geometry of the ligand, its central atom being a sp^3 carbon, square shaped channels (of ~10 Å × 10 Å, running down the *b* direction) are formed inside each layer with the fluorine atoms pointing out from them. These layers, stacking on the [100] direction, are joined by the L2 protonated ligand, which connects two Mn ions related by a translation in the *a* direction and develops the 3D framework.

The proton of the L2 carboxylic group is actually shared with the O1 atom from the neighbour COO^- group of the L1 ligand. The distances O6–H and H–O1 are 1.27(5) and 1.25(5) Å, respectively (see Fig. 3).

In this way, such bonds are between covalent and H-bond interactions in nature, indicating that there are two electrons delocalized between the three atomic centers: O6–H–O1. The resultant 3D MOF consists of infinite chains of MnO_5–C–MnO_5 square pyramid polyhedra as the SBUs, connected in the *a* and *c* directions by the L1 and L2 linkers.

As can be seen in Fig. 3 and 5 (middle), the pyramids are rotated ~90° one to each other and the bidentate-bridge carboxylate groups exhibit a *syn-anti* geometry. As a result, the Mn···Mn distance in the SBU is 4.058(1) Å. A similar SBU based on penta-coordinated Mn ions was reported in a 3D coordination framework of the related ligand 4,4′-(hexafluoroisopropylidene)diphthalic

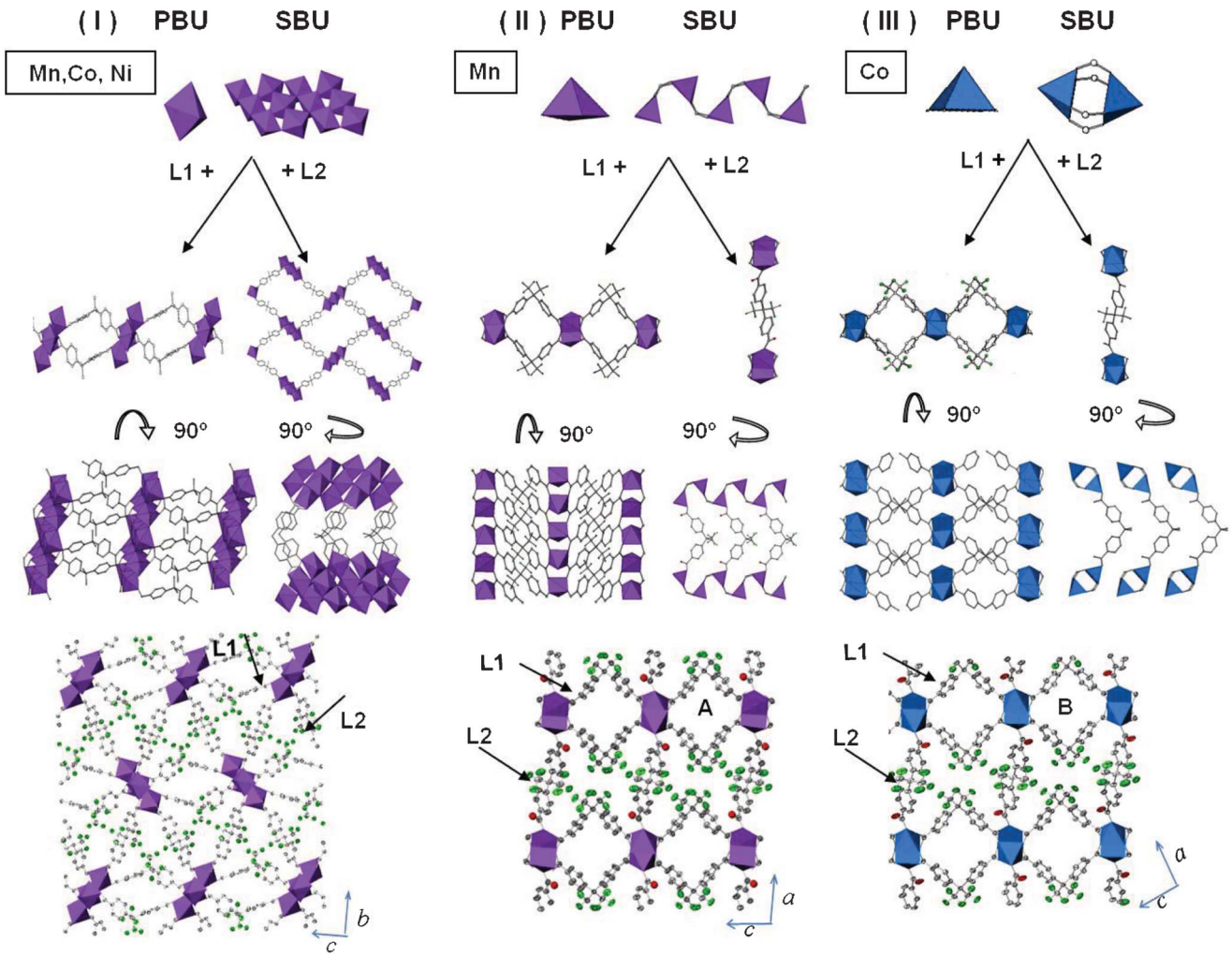

Fig. 5 Packing of the three structural types, showing the primary and secondary building units (PBUs and SBUs).

acid.[22] However in that case the Mn ions adopt a pseudo-tetrahedral geometry and the shortest Mn···Mn distance inside the chain is 3.719(1) Å, being shorter than the corresponding distance of compound **2**. This difference could be related to the fact that all carboxylate groups coordinate in a *syn-syn* bidentate-bridge mode allowing for metal centers to approach more closely than in compound **2**.

[Co_2(hfipbb)$_2$(H_2hfipbb)] (3). This compound was recently presented by Jiang and Xu[23] and is isostructural with that of copper.[24] Moreover another compound with formula [Co_2(hfipbb)$_2$(H_2hfipbb)(H_2O)] has also been reported.[25] Apart from the water molecule, whose nature is not described in ref. 25, and the fact that the structure was solved as *P2/c* instead of *P2/n* as in our case, the compound seems to be the same. For these reasons, here we briefly describe the crystal structure of **3** in order to compare with the novel compound, **2**. In **3** neither coordination nor hydration water molecules are present. In any case, the synthesis methodology reported here (see Supporting Information†) is substantially different and allows for a yield, purity and reproducibility that the authors of ref. 25 say was not possible to achieve with their synthesis procedure.

As in compound **2**, the asymmetric unit of **3** comprises one pentacoordinated Co(II) ion, with square pyramidal geometry, and one and a half non-equivalent ligands, one of which is completely deprotonated (L1) and the remaining half one is protonated (L2) (Figure S4†).

There are important differences between these two frameworks: firstly, the CoO_5 pyramids are fronted by their quadrangular faces forming isolated paddle-wheel dimeric units instead of chains. Secondly, although in this framework the square channelled thick layers are formed by dimer connections through L1 (Fig. 5, right column), the way in which L1 connects them is quite different. While in **2** the chains are connected in a parallel way by the *syn-anti* bis(bidentate bridge) L1 ligand (B type), in **3** the dimers are connected in a crossing-edges way, L1 being in a *syn-syn* bis(bidentate bridge) mode, which gives rise to quite similar channels in size and shape, but with different walls (A type).[21] The layers, which in this case stack along the [101] direction, are joined by the L2 protonated ligand, that also acts as bis(mondentate) linker.

Regarding the different constitution of layers in **2** and **3**, it is interesting to note that Du *et al.* have recently reported a quite similar compound with formula [Cu(hfipbb)(H_2O)] among other less similar MOFs.[26] In such a case the copper hybrid framework consists of a 2-fold interpenetrated net with 1D tubular channels constructed from 2_1 double-stranded helical chains in alternate left- and right-handed fashion. Moreover, they have observed that the smaller dihedral angles between aromatic rings (61.3–73.8°) favour the formation of helical coordination arrays. In our case, while in **3** it is possible to observe an analogous layer formed by 2_1 double-stranded helical chains connected in the same alternating manner, in **2**, the parallel disposition of the L1 ligand avoids the helical arrangement. Furthermore, as can be seen in Scheme 1 (bottom), the ω angle in **2** is smaller (68.79°) than that of L1 in **3** (72.99°), both values being within the empirical range observed by the authors in ref. 26. However, in our case only compound **3** exhibits a helical array, probably due to the difference in the ligand disposition and carboxylate geometry.

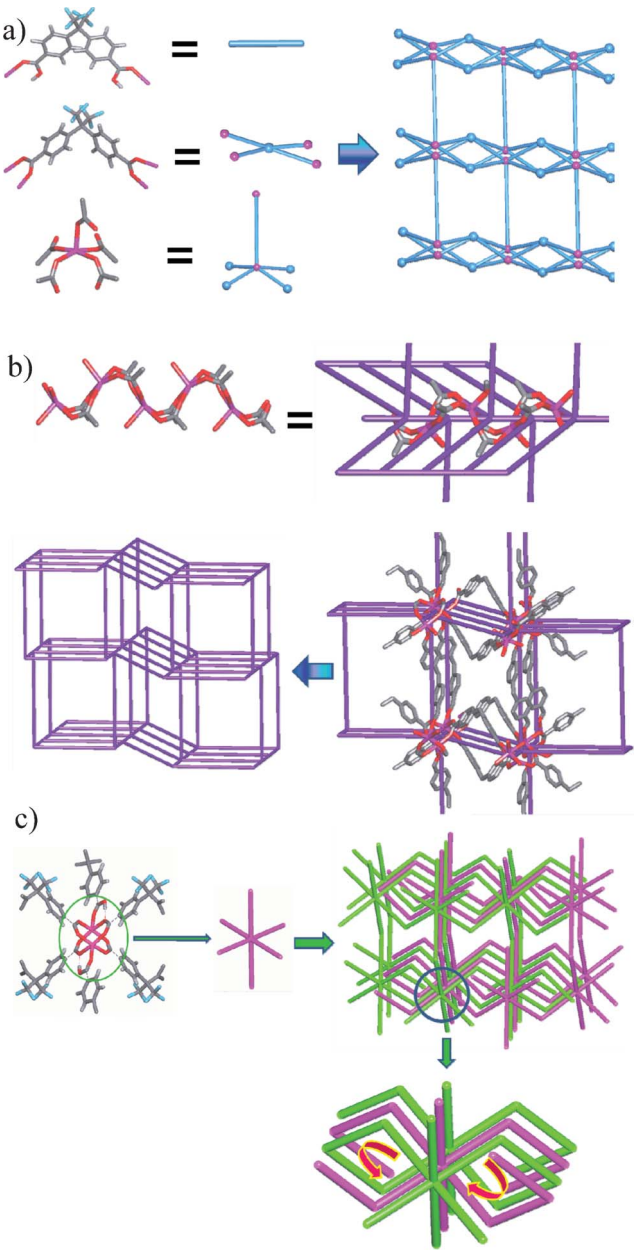

Fig. 6 a) Standard simplification of compound **2** giving the **tcs** topological type; b) rod-packing description of **2** giving a **bnn** type; c) cluster simplification of compound **3** and the corresponding 2-fold interpenetrated **pcu** net.

Taking into account the essential similarity between the structures of compounds **2** and **3** (equal composition of the asymmetric unities, the same coordination modes of the ligands and the same coordination number of the metal centres) but, in turn, the different resultant space groups, we were interested in the analysis of the structural reasons for such a difference from a topological point of view. Consequently, the incidence of the different geometries of coordinated carboxylate groups (*syn-anti* in **2** and *syn-syn* in **3**) and the dissimilar SBUs in the resultant network topology was studied using the TOPOS program.[27]

Fig. 6a shows the standard simplification of compound **2**, in which the Mn ion is a 5-connected node, L1 is a 4-connected one and L2 acts as a linker, lead to a binodal net, corresponding to the "**tcs**" topological type.

On the other hand, if one considers the infinite –MnO_5–C–MnO_5– chains as rod-shaped SBUs, the structure should be related to the square packing of the parallel rods. The associated net for this rod geometry is a 6-coordinated **pcu**, but in this case, the only possible alternative simplification gives rise to a 5-connected **bnn** net. In this simplified net, which is a subnet of **pcu**, each node is located at the centroid position between adjacent Mn ions (see Fig. 6b) and is linked to another two nodes inside the chain and to another three nodes in squared parallel chains through three ligands (two L1 and one L2). This topology simply characterizes the packing of the SBUs but does not reflect the topological role of the hfipbb ligands. One could treat **bnn** as an underlying net only if the internal structure of the polymeric chains is ignored,[28] while with the standard simplification procedure this feature is properly taken into account. However, the rod-shaped SBU packing is also important because it has been associated with avoiding net interpenetration and is helpful for the design and synthesis of metal organic frameworks.[29]

The simplified net of compound **3** consists of hexa-coordinated nodes located at the centroid of the paddle-wheel cluster giving rise to a 2-fold interpenetrated **pcu** net (Fig. 6c).

3.2 X-ray powder diffraction studies

Attempts to perform the structure resolution using single crystal X-ray diffraction data for compounds **1b** and **1c** were hindered by difficulties in obtaining suitable single crystals. For that reason, powder diffraction methods including Rietveld analysis were applied in order to confirm the isostructural character of these compounds with **1a**. Moreover, the obtained results allow for verifying the purity of the three compounds.

The structural model employed for this purpose was based on cell parameters and atomic positions of compound **1a** obtained from single crystal synchrotron X-ray diffraction data at 100 K. The first step in the present study was refinement by Rietveld analysis of the **1a** structural model, considering the T = 298 K.

Then, a similar procedure was carried out using this model to obtain the refined cell parameters, at the same temperature, for compounds **1b** and **1c**; the obtained results for **1a–c** compounds are shown in Figure S5,† Table 2 and Tables S1–S3.†

As can be seen in Figure S5,† the concordance between the simulated and observed patterns shows not only the isostructural character of compounds **1a–c** but also confirms the purity of the samples (no additional peaks are observed in the experimental data). Besides, the variations in the cell parameters and volumes from compound **1a** to **1c** are in accordance with the observed reduction in the ionic radii from Mn(II) to Ni(II) ions. The resultant intermetallic distances for refined structural models are displayed in Table 3.

Table 2 Refined cell parameters for compounds **1a–1c** from Rietveld analysis. In the case of **1a**, the cell parameters determined by single crystal data at 100 K are also presented (denoted as **1a***)

	a/Å	b/Å	c/Å	β (°)	V/Å^3
1a*	7.227(2)	31.837(6)	16.434(3)	99.98(3)	3749.8(1)
1a	7.316(2)	32.023(5)	16.533(3)	99.91(2)	3816(1)
1b	7.127(1)	31.803(4)	16.424(2)	99.89(2)	3667.5(9)
1c	7.085(2)	31.766(7)	16.404(4)	99.78(4)	3638(2)

3.3 Magnetic properties

The temperature dependence of the dc magnetic susceptibility, χ, for **1a** (Fig. 7) obeys the Curie–Weiss law

$$\chi = \frac{C}{T-\theta}$$

between 120 and 300 K. The fit of the data yields a Weiss temperature (θ) value of -90.5 ± 0.4 K, indicating predominant antiferromagnetic interactions between the Mn^{2+} metal atoms. In fact the smooth positive deviation from the Curie–Weiss law observed in the χ^{-1} *vs.* T plot below 100 K could be attributed to operating antiferromagnetic interactions. Unfortunately, χ does not reach the expected maximum corresponding to such antiferromagnetic interactions because of a sudden jump observed at 46 K. Such a jump, followed by a maximum at 40 K, is indicative of the presence of Mn_3O_4 oxide as an impurity because it behaves as a ferrimagnet with a Curie temperature of 42 K.[30] At this point it is important to

Table 3 Intermetallic distances for compound **1a–c**

1a	Intermetallic distances[a]
Mn1···Mn4[b]	3.189 (3.1701(9)[c])
Mn1···Mn2	3.558 (3.540(1)[c])
Mn2···Mn3[b]	3.525 (3.5029(9)[c])
Mn3···Mn4	3.658 (3.6385(8)[c])
Mn3···Mn1	3.523 (3.5040(9)[c])
Mn2···Mn4	3.710 (3.690(1)[c])
Mn2···Mn1	3.801 (3.780(1)[c])
$(Mn\cdots Mn)_{average}$	3.566
$(Mn\cdots Mn)_{interchain}$ (along c)	16.532
$(Mn\cdots Mn)_{interchain}$ (along b)	32.023
1b	
Co1···Co4*	3.152
Co1···Co2	3.468
Co2···Co3*	3.484
Co3···Co4	3.564
Co3···Co1	3.478
Co2···Co4	3.668
Co2···Co1	3.703
$(Co\cdots Co)_{average}$	3.502
$(Co\cdots Co)_{interchain}$ (along c)	16.424
$(Co\cdots Co)_{interchain}$ (along b)	31.803
1c	
Ni1···Ni4*	3.146
Ni1···Ni2	3.448
Ni2···Ni3*	3.477
Ni3···Ni4	3.543
Ni3···Ni1	3.467
Ni2···Ni4	3.658
Ni2···Ni1	3.681
$(Ni\cdots Ni)_{average}$	3.488
$(Ni\cdots Ni)_{interchain}$ (along c)	16.404
$(Ni\cdots Ni)_{interchain}$ (along b)	31.766

[a] The displayed intermetallic distances come from the Rietveld analysis of the PXRD patterns and the standard deviations are not presented because atomic coordinates were not refined. [b] The M1···M4 and M2···M3 distances correspond to the μOH–μOH and μO–μO edge sharing connections, respectively; the other distances are associated with the vertex sharing mode. [c] Intermetallic distances coming from single-crystal analysis using synchrotron radiation diffraction data measured at 100 K.

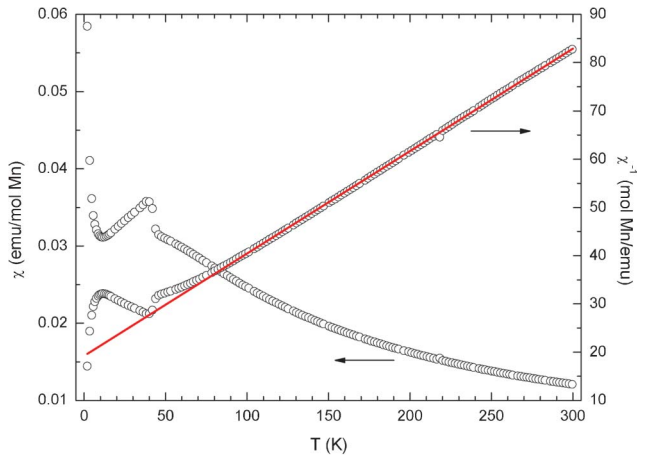

Fig. 7 Thermal variation of χ and χ^{-1} per mol of manganese for compound **1a**. The solid red line corresponds to the Curie–Weiss law fit, yielding $C = 4.710 \pm 0.006$ emu K (mol Mn)$^{-1}$ and $\theta = -90.5 \pm 0.4$ K.

note that SQUID magnetometers are able to detect ppm concentrations of ferro- or ferri-magnetic impurities present in paramagnetic or antiferromagnetic compounds. Such concentrations are not detected by means of others techniques, like powder X-ray diffraction. On the other hand, the thermal evolution of the effective magnetic moment (μ_{eff}), defined as $(8\chi T)^{1/2}$, is shown in Fig. 8. Its value at room temperature is 5.38 μ_B per Mn, lower than the expected spin-only μ_{eff} for Mn^{2+} in octahedral coordination, 5.92 μ_B.[31] Furthermore, the μ_{eff} value decreases progressively down to 0.97 μ_B per Mn at 2 K when it should not vary with temperature for a paramagnetic Mn^{2+} cation. All this confirms the antiferromagnetic interaction between the Mn^{2+} cations, likely intra-triple chain interactions.

The compound **1b** shows paramagnetism from room temperature down to 150 K, following the Curie–Weiss law with $C = 3.432 \pm 0.004$ emu K (mol Co)$^{-1}$ and $\theta = -18.9 \pm 0.3$ K, see Fig. 9.

This negative value of θ may be associated with antiferromagnetic interactions between Co^{2+} ions, but such a value is assigned to a non-interacting octahedral Co^{2+}.[32] Therefore, the

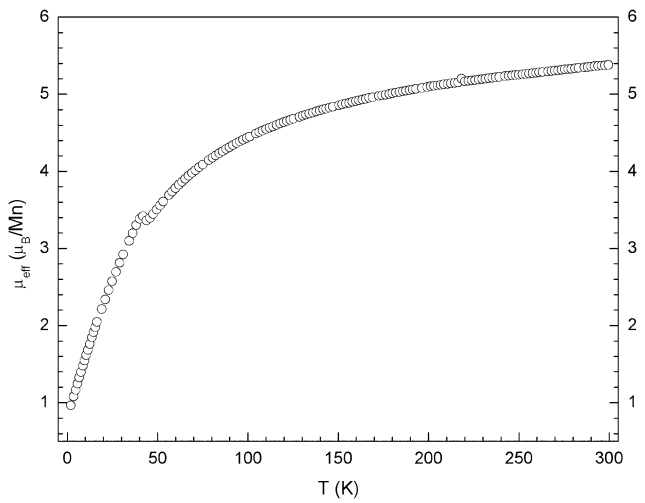

Fig. 8 Temperature dependence of the effective magnetic moment per manganese for compound **1a**.

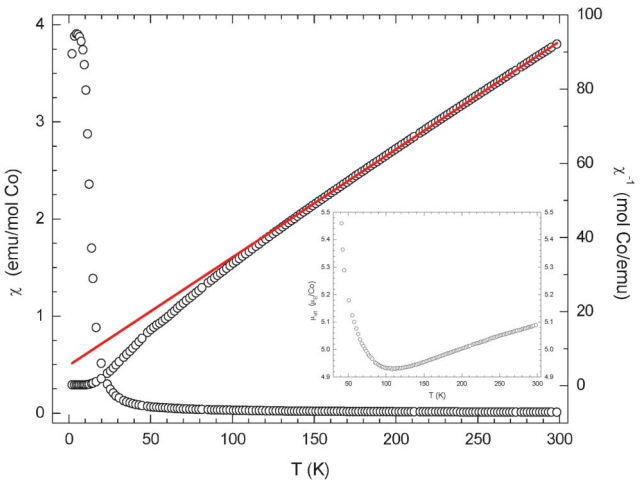

Fig. 9 Thermal variation of χ and χ^{-1} per mol of cobalt for compound **1b**. The solid red line corresponds to the Curie–Weiss law fit. The inset shows the temperature dependence of the effective magnetic moment between 30 and 300 K.

origin of this Curie–Weiss behaviour cannot be ascribed unambiguously to antiferromagnetic interactions. Below 150 K, χ^{-1} presents a negative deviation from the Curie–Weiss law that becomes progressively more noticeable with decreasing temperature. Such behaviour may indicate the appearance of a net magnetization which rises with decreasing temperature. In this sense, a sharp increase of χ is observed at 30 K, followed by a maximum at 4.5 K.

The appearance of this ferromagnetic component is supported by the observed thermal evolution of μ_{eff}, see inset of Fig. 9. It gradually decreases from room temperature (5.09 μ_B per Co) down to 130 K (4.94 μ_B per Co), as expected for a non-interacting octahedral Co^{2+} ion with an $S = 3/2$ configuration and an important orbital contribution. Then, μ_{eff} remains almost constant and, finally, it begins to increase at 100 K.

In order to clarify the origin of this net magnetization, we measured the temperature dependence of the ac magnetic susceptibility, $\chi ac = \chi' - i\chi''$, where χ' is the in-phase inductive

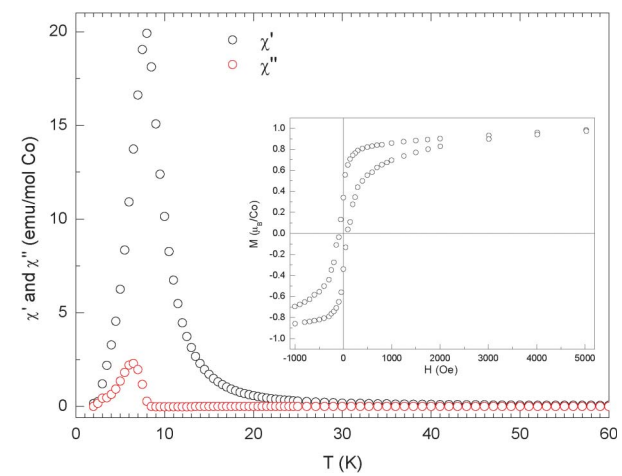

Fig. 10 Thermal variation of ac susceptibility components per mol of cobalt for compound **1b** in the 2–60 K temperature range. The inset shows a zoom of the hysteresis loop obtained at 2 K.

component and χ'' is the out-phase component, see Fig. 10. A sharp peak is observed at 8 K in χ' and χ'' increases at that temperature achieving a maximum at 6.5 K. These signals are frequency independent. This is characteristic of long-range ferromagnetic ordering, suggesting that compound **1b** behaves as a three-dimensional ferromagnet with a Curie temperature T_C near 8 K. Such ferromagnetism is confirmed by the hysteresis loop obtained at 2 K, see inset of Fig. 10. The magnetization is not fully saturated at 5 T but shows a tendency to saturate, reaching 1.56 μ_B per Co at 5 T. This value is smaller than the saturation magnetization expected at low-temperature for a ferro-magnetically coupled six-coordinated high-spin Co^{2+} ion with an effective spin $S = ½$, which is higher than 2 μ_B per Co.[33]

Finally, it is important to note that no maximum in the ac susceptibility components is observed from 30 K up to 180 K (data not shown). This fact could indicate that the previously mentioned net magnetization developed at 100 K may be due to intra-triple chain interactions. The temperature dependence of χ and its inverse for the isostructural nickel compound, **1c**, are plotted in Fig. 11.

From room temperature to ~80 K the observed χ can be fitted to a Curie–Weiss law plus a temperature-independent para-magnetism (TIP) term. The best obtained fit yield $C = 1.1615 \pm 0.0056$ emu K (mol Ni)$^{-1}$, $\theta = 16.68 \pm 0.38$ K and TIP = $0.98 \pm 0.16 \times 10^{-4}$ emu (mol Ni)$^{-1}$. This positive value of θ may be associated with ferromagnetic interactions between Ni^{2+} ions. In fact at ~10 K the χ increases suddenly and then it approaches a constant value at lower temperatures. Concerning μ_{eff}, see inset of Fig. 11, it remains almost constant between 300 and 250 K with a value of 3.18 μ_B per Ni. Such a value agrees with that expected for a compound containing non-interacting six-coordinated Ni^{2+} ions.[34] With decreasing temperature, μ_{eff} increases first very slowly (3.58 μ_B per Ni at 50 K) and then faster (5.43 μ_B per Ni at 10 K).

The onset of a maximum at 2.5 K in χ' and the increase of the χ'' at 2.5 K, see Fig. 12, indicates the existence of long-range ferromagnetic interactions with a critical temperature T_C of 2.5 K. The hysteresis loop obtained at 2 K confirms such magnetic behaviour, see inset of Fig. 12. The magnetization

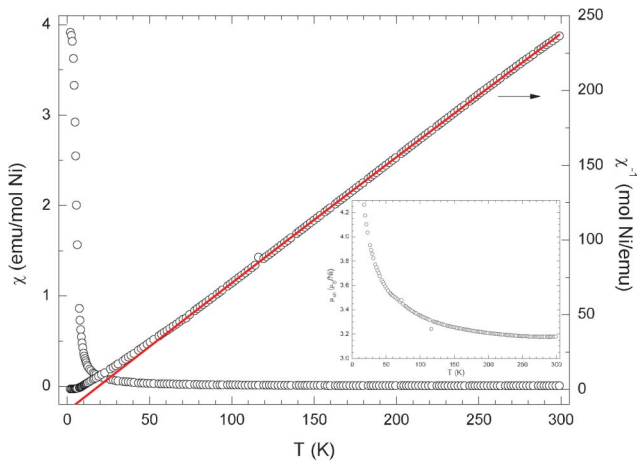

Fig. 11 Thermal variation of χ and χ^{-1} per mol of nickel for compound **1c**. The solid red line corresponds to the Curie–Weiss law fit. The inset shows a zoom of effective magnetic moment *vs.* temperature plot.

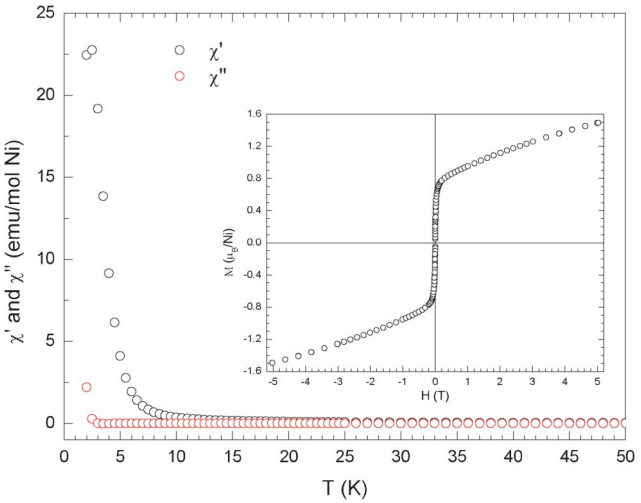

Fig. 12 Thermal variation of ac susceptibility components per mol of nickel for compound **1b**. The inset shows the hysteresis loop obtained at 2 K.

increases rapidly to reach 0.97 μ_B per Ni at 10 kOe, then it increases linearly up to 20 kOe before it deviates towards saturation, reaching 1.49 μ_B per Ni at 50 kOe. This value is lower than the expected saturation magnetization of about 2 μ_B per Ni corresponding to a Ni^{2+} with a spin of $S = 1$ according to $M_{sat} = gS$ where g is the Landé factor and S is the spin quantum number.

Compound **2**, with MnO_5 square pyramids as the PBU forming chains along the b direction, follows a Curie–Weiss law above 100 K, see Fig. 13. The θ value indicates very weak antiferromagnetic interactions between Mn^{2+} ions. In this sense, the experimental μ_{eff} obtained at room temperature, 5.79 μ_B per Mn, is very close to that expected for the spin-only case, *i.e.* 5.92 μ_B with $S_{Mn} = 5/2$. χ shows a small jump at 45 K, which indicates the presence of Mn_3O_4 oxide as an impurity, as in the case of compound **1a**. Finally, the appearance of a net maximum

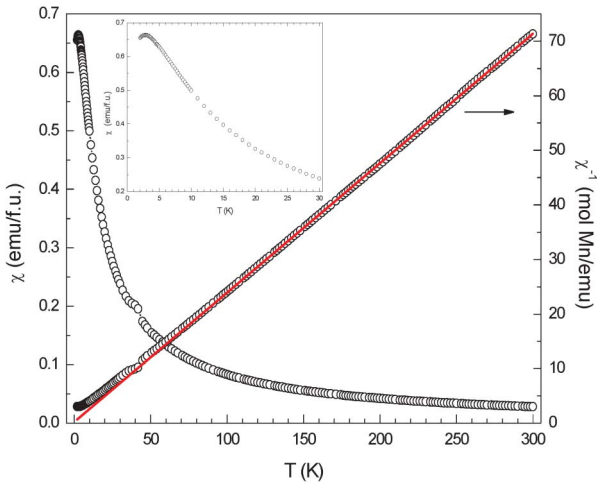

Fig. 13 Thermal variation of χ per formula unit and χ^{-1} per mol of manganese for compound **2**. The solid red line corresponds to the Curie–Weiss law fit, yielding $C = 4.211 \pm 0.003$ emu K (mol Mn)$^{-1}$ and $\theta = -0.77 \pm 0.15$ K. The inset shows the temperature dependence of χ at low temperature.

at 2.8 K, see inset of Fig. 13, confirms weak antiferromagnetic interactions in **2**. The Mn_3O_4 impurity precludes the use of an analytical expression in order to study the intra- and interchain interactions that can be present. However, taking into account the intrachain Mn···Mn distance (~ 4.06 Å) and the two shortest interchain Mn···Mn separations (~11.6 Å along the *c* direction, and ~14.4 Å along the *a* direction of the structure) we can assign the onset of intrachain magnetic interactions as the origin of the mentioned maximum.

The magnetic behaviour of compound **3**, with CoO_5 square pyramids as the PBU forming isolated paddle-wheel cobalt(II) binuclear units, is characterized by the onset of a maximum at 18 K in χ, see Fig. 14. Such a feature denotes antiferromagnetic interactions between the two metal centres with a T_N near 18 K. The higher ordering temperature found in **3** with respect to that of **2** is in agreement with the shorter metal···metal distance inside the paddle wheel CoO_5–C–CoO_5 (2.9157 Å) in comparison with that found between Mn ions inside the MnO_5–C–MnO_5 chains (4.0582 Å). Besides, the *syn-syn* geometry of the carboxylate groups favours stronger interactions than in the case of the *syn-anti* one.[35] In this way, the disposition of the OCO groups in the paddle-wheel cluster in **3** demonstrates a better coupling than that present in the *syn-anti* Mn–OCO–Mn–OCO–Mn infinite chain, resulting in a higher T_N in the case of **3**.

Below 6 K, χ increases indicating the presence of a paramagnetic impurity. Above 60 K compound **3** follows the Curie–Weiss law with $C = 3.445 \pm 0.002$ emu K (mol Co)$^{-1}$ and $\theta = -31.6 \pm 0.1$ K, and the experimental μ_{eff} obtained at room temperature is 5.0 μ_B per Co. This value is larger than the spin-only value expected for a $^4A_2$ ground state, but spin–orbit coupling and $^4A_2(P)$–$^4A_2(F)$ mixing justify the observed room-temperature μ_{eff}.[36] The temperature dependence of μ_{eff} is shown in the inset of Fig. 14. The best fit of the magnetic susceptibility data of binuclear compound **3**, see Fig. 14, is obtained taking into account the monomer magnetic susceptibility with the single-ion zero-field splitting (ZFS) effect, and the magnetic exchange between the two interacting Co^{2+} ions. This model corresponds to the following expressions:[37]

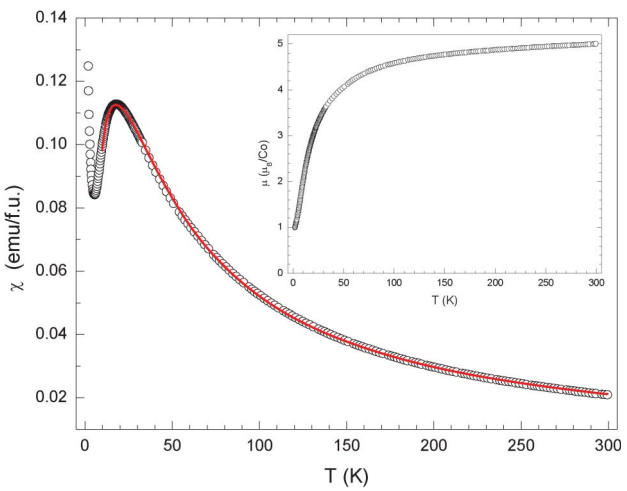

Fig. 14 Thermal variation of experimental (circles) and calculated (solid line) magnetic susceptibility per formula unit for compound **3**. The inset shows the temperature dependence of μ_{eff}.

$$\chi_z = \frac{Ng_z^2\beta^2}{4kT}\frac{1+9\exp(-D/kT)}{1+\exp(-D/kT)}$$

$$\chi_x = \frac{Ng_x^2\beta^2}{4kT}\frac{4+(6kT/D)-(6kT/D)\exp(-D/kT)}{1+\exp(-D/kT)}$$

$$\chi = \frac{\chi_z+2\chi_x}{3}\times 2\times\frac{6}{3+\exp(-25J/9kT)}+\mathrm{TIP}$$

for parallel, perpendicular and average magnetic susceptibilities, respectively, where N is the Avogadro number, k is the Boltzmann constant, β is the Bohr magneton and T is temperature. D (the ZFS parameter), J (the exchange parameter), g_z and g_x (the parallel and perpendicular Landé factors, respectively) and TIP (a temperature-independent paramagnetism term) are the fitting parameters. The best fit of the data was achieved in the 9–300 K temperature range, that is, the paramagnetic impurity was not considered by an additional term in the χ expression, and the best-fit values obtained were $g_z = 3.152 \pm 0.008$, $g_x = g_y = 1.21 \pm 0.01$, $D = 34.3 \pm 0.4$ cm^{-1} (the $\pm 1/2$ state is lower in energy than the $\pm 3/2$ state), $J = -13.54 \pm 0.08$ cm^{-1} and TIP = $2.16 \pm 0.01 \times 10^{-3}$ emu per f.u.

3.4 Thermal analysis

TGA and DTA curves for compounds **1a–c**, **2** and **3** are shown in Fig. S6–S10.†

$[Mn_3(hfipbb)_2(OH)_2(H_2O)]$ (**1a**): Dehydration proceeds in one stage with a weight loss of 2% (calc. 1.8%) consistent with the removal of the coordinated water molecule. The second step in the TGA curve is accompanied by a strong exothermic DTA signal centered at 414 °C and corresponds to the complete decomposition of the anhydrous compound. The calculated weight loss for the whole process (77.06%) is in good agreement with the experimental value of 78.12%. The final product was characterized by PXRD and was identified as tetragonal Mn_3O_4.[38]

The thermal behaviour of $[Co_3(hfipbb)_2(OH)_2(H_2O)]$ (**1b**) and $[Ni_3(hfipbb)_2(OH)_2(H_2O)]$ (**1c**) was identical to that of compound **1a**. The experimental weight losses for the first step were 1.71% and 2.3%, for **1b** and **1c**, respectively; these values are in agreement with the calculated one of 1.78%.

For compound **1b**, the decomposition of the anhydrous compound is reflected in the DTA curve as a strong exothermic peak centered at ~395 °C, leaving as a final residue the spinel type Co_3O_4.[39] The calculated weight loss for the whole process (76.14%) is in good agreement with the experimental value of 76.6%. For compound **1c**, the DTA signal corresponding with the decomposition process is centered at ~435 °C. The final residue was identified as cubic NiO,[40] the calculated weight loss for the whole process (77.8%) being in good agreement with the experimental value of 79.2%.

Regarding the fact that compounds **1a–c** have a coordinated water molecule, we were interested in the structural stability after the dehydration process. In this way, a sample of **1c**, whose water molecule is lost at the highest temperature, was heated at 250 °C in air and an XRD powder pattern was registered at the end of the thermal treatment. As can be seen in Fig. S11† no evidence of structural collapse is observed.

[Mn_2(hfipbb)$_2$(H_2hfipbb)] (2). The first mass loss begins at ~200 °C to ~400 °C and represents a 9.33% loss. It is probably due to the removal of both protonated carboxylate groups of the L2 ligand to give two CO_2 molecules and a water molecule (calculated weight loss = 8.27%). A weak exothermic DTA signal is observed at 365 °C.

Above 300 °C the decomposition of compound **2** occurs, and the corresponding mass loss is about 78.45% giving as a final product tetragonal Mn_3O_4.[35] The calculated weight loss for the whole process (88.10%) is in very good agreement with the experimental value (87.58%). The DTA curve shows a very complex signal above 400 °C. However, using a slower heating rate (see Fig. S9-b† and experimental section), it is possible to resolve the overlapping peaks and three clear exothermic signals are detected at 345, 375 and 437 °C. The first one is associated with the dehydrodecarboxylation of the L2 ligand, and the following ones with the main degradation processes of the compound.

[Co_2(hfipbb)$_2$(H_2hfipbb)] (3). The compound exhibits good thermal stability due to the fact that it is neither hydrated nor has coordinated water molecules. The decomposition of this compound begins at ~300 °C, being the first DTA peak centred at 380 °C. After that, another two steps of weight loss take place, which are denoted by two strong exothermic peaks in the DTA curve centred at ~430 and ~460 °C. The characterization of the residue obtained at 900 °C allowed the identification of spinel type Co_3O_4[28] as a final product and the calculated weight loss for the whole process (87.56%) is in good agreement with the experimental value of 88.39% (see Fig. S10†).

3.5 Infrared spectroscopy

The FTIR spectra of compounds **1a–c**, **2** and **3** are displayed in the Supporting Information, Fig. S12 and S13.† The spectra of compounds **1a–c** show three sharp bands of medium intensity located at 3635, 3615 and 3470 cm^{-1}; the first two of them are assigned to the O–H stretching mode of (OH) groups, while the third one is assigned to the same mode of the coordinated water molecule. In the case of the spectra of compounds **2** and **3**, no bands appear in this zone, which is consistent with the absence of water molecules in the structure (see Figure S13†).

Spectra of all compounds show a weak band at 3060 cm^{-1}, which is assigned to the C–H stretching mode of aromatic rings. In the region of 1605–1400 cm^{-1} there are several strong bands that include the stretching υ_{as}(OCO) mode and υ(CC) aromatic skeletal vibrations. In the spectra of compounds **2** and **3**, there are two additional medium and strong bands located at 1655 and 1640 in **2**, and 1655 and 1630 cm^{-1} in **3**, which are assigned to the stretching υ_{as}(OCO) mode of the coordinated protonated carboxylic groups of the L2 ligand.

In the 1390–1325 cm^{-1} range of all spectra, there are several strong and medium bands assigned to the υ(CF) stretching vibration, while in the 750–690 cm^{-1} zone, the $\upsilon(CF_3)$ bending vibration appears as medium bands. In the 490–420 cm^{-1} range there are some medium and weak bands that could be assigned to the υ(M–O) stretching vibrations.

Conclusions

Five novel metal organic frameworks, belonging to three structural types, have been obtained hydrothermally. The higher synthesis temperatures and higher pH values led for obtaining three compounds with formula [M_3(hfipbb)$_2$(OH)$_2$(H_2O)], (M = Mn, Co, Ni) that belong to the first structural type with high metal–oxygen condensation, giving M_3O_{14} triple-chain based SBUs. The crystal structure of the Mn-based compound was obtained from single crystal synchrotron X-ray diffraction data, while for the other three compounds conventional powder X-ray diffraction methods confirmed the isostructural character with the Mn-based compound for all of them. On the contrary, the milder hydrothermal synthesis conditions and lower pH values resulted in a rod-shaped MnO_5–C–MnO_5 or paddle-wheel CoO_5–C–CoO_5 SBUs in compounds **2** and **3**, respectively. The magnetic behaviour of compounds [M_3(hfipbb)$_2$(OH)$_2$(H_2O)] with M = Co and Ni is characterized by the onset of long-range ferromagnetic order at very low temperature, with Curie temperatures near 8 and 2.5 K, respectively. Such spontaneous magnetization seems to be preceded by low-dimensional magnetic interactions, due to the nature of the secondary building units of the structure, which are triple chains built by M_3O_{14} units. In the case of the compound with M = Mn, the presence of a small amount of the ferrimagnetic Mn_3O_4 oxide precludes the magnetic characterization of the compound from 50 K down to 2 K, but below 100 K intra-chain antiferromagnetic interactions seem to be operative. Concerning compounds [M_2(hfipbb)$_2$(H_2hfipbb)] with M = Mn and Co, with structural type **2** and **3**, the antiferromagnetic interactions observed at very low temperature (magnetic susceptibility maximum at 2.8 and 18 K, respectively) are confined to the secondary building units. In these cases, not only the intermetallic distances but also the *syn-syn* or *syn-anti* carboxylate geometries drive the magnetic couplings.

Acknowledgements

This work has been supported by the Spanish MCYT Project MAT2010-17571, S2009/MAT-1756/CAM and Consolider-Ingenio CSD2006–2010. The authors are grateful for the financial support for beam time at the BM16 Spanish beam line-ESRF (proposal N° 16-01-741). A. E. P. P. acknowledges a JAE fellowship from CSIC and Fondo Social Europeo from the EU.

References

1 (*a*) G. Férey, *Chem. Soc. Rev.*, 2008, **37**, 191; (*b*) U. Mueller, M. Schubert, F. Teich, H. Puetter, K. Schierle-Arndt and J. Pastré, *J. Mater. Chem.*, 2006, **16**, 626; (*c*) A. U. Czaja, N. Trukhanb and U. Müller, *Chem. Soc. Rev.*, 2009, **38**, 1284.
2 (*a*) A. E. Platero-Prats, V. A. de la Peña-O'Shea, M. Iglesias, N. Snejko, A. Monge and E. Gutiérrez-Puebla, *ChemCatChem*, 2010, **2**, 147; (*b*) A. E. Platero-Prats, V. A. de la Peña-O'Shea, M. Iglesias, N. Snejko, A. Monge and E. Gutiérrez-Puebla, *Chem.–Eur. J.*, 2010, **16**, 11632.
3 A. Monge, N. Snejko, E. Gutiérrez-Puebla, M. Medina, C. Cascales, C. Ruiz-Valero, M. Iglesias and B. Gómez-Lor, *Chem. Commun.*, 2005, 1291.
4 F. Gándara, B. Gómez-Lor, E. Gutiérrez-Puebla, M. Iglesias, M. A. Monge, D. M. Proserpio and N. Snejko, *Chem. Mater.*, 2008, **20**, 72.

5 F. Gándara, A. de Andrés, B. Gómez-Lor, E. Gutiérrez-Puebla, M. Iglesias, M. A. Monge, D. M. Proserpio and N. Snejko, *Cryst. Growth Des.*, 2008, **8**(2), 378.
6 F. Gándara, V. de la Peña ÓShea, F. Illas, N. Snejko, D. M. Proserpio, E. Gutiérrez-Puebla and M. A. Monge, *Inorg. Chem.*, 2009, **48**, 4707.
7 (*a*) M. Tonigold, Y. Lu, B. Bredenkötter, B. Rieger, S. Bahnmüller, J. Hitzbleck, G. Langstein and D. Volkmer, *Angew. Chem., Int. Ed.*, 2009, **48**, 7546; (*b*) R. Sen, S. Bhunia, D. Mal, S. Koner, Y. Miyashita and K.-I. Okamoto, *Langmuir*, 2009, **25**(23), 13667; (*c*) S.-H. Cho, B. Ma, S. T. Nguyen, J. T. Hupp and T.E. Albrecht-Schmitt, *Chem. Commun.*, 2006, 2563.
8 (*a*) C.-Y. Sun, S. Gao and L.-P. Jin, *Eur. J. Inorg. Chem.*, 2006, 2411; (*b*) D. Maspoch, D. Ruiz-Molina, K. Wurst, N. Domingo, M. Cavallini, F. Biscarini, J. Tejada, C. Rovira and J. Veciana, *Nat. Mater.*, 2003, **2**, 190; (*c*) H. Srikanth, R. Hajndl, B. Moulton and M. J. Zaworotko, *J. Appl. Phys.*, 2003, **93**, 10Parts 2 &3, 7089.
9 D. Maspoch, D. Ruiz-Molina and J. Veciana, *J. Mater. Chem.*, 2004, **14**, 2713.
10 X.-Y. Wang, Z.-M. Wang and S. Gao, *Chem. Commun.*, 2007, 1127.
11 (*a*) S. J. Blundell and F. L. Pratt, *J. Phys.: Condens. Matter*, 2004, **16**, R771–R828; (*b*) Molecular Magnetism, *New Magnetic Materials*, ed. K. Itoh and M. Kinoshita, Gordon Breach-Kodansha, Tokyo, 2000.
12 M. Kurmoo, *Chem. Soc. Rev.*, 2009, **38**, 1353.
13 N. Snejko, E. Gutiérrez-Puebla, J. L. Martínez, M. A. Monge and C. Ruiz-Valero, *Chem. Mater.*, 2002, **14**, 1879.
14 L. J. Smith, H. Eckert and A. K. Cheetham, *J. Am. Chem. Soc.*, 2000, **122**, 1700.
15 Z. Otwinowski and W. Minor, *Processing of X-ray Diffraction Data Collected in Oscillation Mode, Methods in Enzymology*, Volume **276**: Macromolecular Crystallography, part A, ed. C. W. Carter, Jr. and R. M. Sweet, Academic Press, New York, 1997, pp. 307–326.
16 *Siemens SAINT data collection and procedure software for the SMART system*, Siemens Analytical X-ray Instruments, Inc., Madison, WI, 1995.
17 *Siemens SHELXTL, version 5.0*, Siemens Analytical X-ray Instruments Inc., Madison, WI, 1995.
18 E. Dowty, ATOMS for Windows 3.1, *a computer program for displaying atomic structure*, Kingsport, TN, 1995.
19 Materials Studio Modelling 4.4, http://www.accelerys.com/mstudio/ms_modeling..
20 G. A. Bain and J. F. Berry, *J. Chem. Educ.*, 2008, **85**(4), 532.
21 (*a*) A. Monge, N. Snejko, E. Gutiérrez-Puebla, M. Medina, C. Cascales, C. Ruiz-Valero, M. Iglesias and B. Gómez-Lor, *Chem. Commun.*, 2005, 1291; (*b*) F. Gándara, M. Medina, N. Snejko, E. Gutiérrez-Puebla, D. M. Proserpio and M. A. Monge, *CrystEngComm*, 2010, **12**, 711; (*c*) F. Gándara, A. de Andrés, B. Gómez-Lor, E. Gutiérrez-Puebla, M. Iglesias, M. A. Monge, D. M. Proserpio and N. Snejko, *Cryst. Growth Des.*, 2008, **8**, 378; (*d*) F. Gándara, V. A. de la Peña-O'Shea, F. Illas, N. Snejko, D. M. Proserpio, E. Gutiérrez-Puebla and M. A. Monge, *Inorg. Chem.*, 2009, **48**, 4707.
22 R.-Q. Zhong, R.-Q. Zou, M. Du, T. Yamada, G. Maruta, S. Takeda and Q. Xu, *Dalton Trans.*, 2008, 2346.
23 H. Jiang and Q. Xu, *CrystEngComm*, 2010, **12**, 3815.
24 L. Pan, M. B. Sander, X. Huang, J. Li, M. Smith, E. Bittner, B. Bockrath and J. K. Johnson, *J. Am. Chem. Soc.*, 2004, **126**, 1308.
25 C. Ji, L. Huang, J. Li, H. Zheng, Y. Lib and Z. Guo, *Dalton Trans.*, 2010, **39**, 8240.
26 X.-J. Jiang, S.-Z. Zhang, J.-H. Guo, X.-G. Wang, J.-S. Li and M. Du, *CrystEngComm*, 2009, **11**, 855.
27 (*a*) V. A. Blatov, *IUCr Compcomm Newsl.*, 2006, **7**, 4; (*b*) V. A. Blatov, L. Carlucci, G. Ciani and D. M. Proserpio, *CrystEngComm*, 2004, **6**, 378.
28 E. V. Alexandrov, V. A. Blatov, A. V. Kochetkov and D. M. Proserpio, *CrystEngComm*, 2011, **13**, 3947.
29 N. L. Rosi, J. Kim, M. Eddaoudi, B. Chen, M. O'Keeffe and O. M. Yaghi, *J. Am. Chem. Soc.*, 2005, **127**, 1504.
30 K. Dwight and N. Menyuk, *Phys. Rev.*, 1960, **119**(5), 1470.
31 B. N. FiggisM. A. Hitchman, *Ligand Field Theory and Its Applications*, Wiley-VCH, New York, 2000.
32 F. E. MabbsD. J. Machin*Magnetism and Transition Metal Complexes*, Dover Publications, Toronto, 2008.
33 F. Lloret, M. Julve, J. Cano, R. Ruiz-García and E. Pardo, *Inorg. Chim. Acta*, 2008, **361**, 3432.
34 P. Mahata, D. Sarma and S. Natarajan, *J. Chem. Sci.*, 2010, **122**(1), 19.
35 H. Lisura and T. Nagata, *Inorg. Chem.*, 1998, **37**, 4702.
36 D.M. Duggan and D.N. Hendrickson, *Inorg. Chem.*, 1975, **14**(8), 1944.
37 N. Duran, W. Clegg, L. Cucurull-Sánchez, R. A. Coxall, H. R. Jiménez, J. M. Moratal, F. Lloret and P. González-Duarte, *Inorg. Chem.*, 2000, **39**, 4821.
38 V. Baron, J. Gutzmer, H. Rundlof and R. Tellgren, *Am. Mineral.*, 1998, **83**, 786.
39 W. M. Shaheen and A. A. Ali, *Mater. Res. Bull.*, 2001, **36**, 1703.
40 H. Taguchi, *Solid State Commun.*, 1998, **108**, 635.